

Turbulence spreading effects on the ELM size and SOL width

Nami Li^{1,†}, X.Q. Xu¹, P.H. Diamond², Y.F. Wang³, X. Lin³, N. Yan³ and G.S. Xu³

¹Lawrence Livermore National Laboratory, Livermore, CA 94550, USA

²University of California San Diego, La Jolla, CA 92093-0429, USA

³Institute of Plasma Physics, Chinese Academy of Sciences, Hefei 230031, PR China

(Received 10 August 2023; revised 29 January 2024; accepted 30 January 2024)

BOUT++ turbulence simulations were performed to investigate the impact of turbulence spreading on the edge localized mode (ELM) size and divertor heat flux width (λ_q) broadening in small ELM regimes. This study is motivated by EAST experiments. BOUT++ linear simulations of a pedestal radial electric field (E_r) scan show that the dominant toroidal number mode (n) shifts from high- n to low- n , with a narrow mode spectrum, and the maximum linear growth rate increases as the pedestal E_r well deepens. The nonlinear simulations show that as the net $E \times B$ pedestal flow increases, the pressure fluctuation level and its inward penetration beyond the top of the pedestal both increase. This leads to a transition from small ELMs to large ELMs. Both inward and outward turbulence spreading are sensitive to the scrape-off-layer (SOL) plasma profiles. The inward turbulence spreading increases for the steep SOL profiles, leading to increasing pedestal energy loss in the small ELM regime. The SOL width (λ_q) is significantly broadened progressing from the ELM-free to small ELM regime, due to the onset of strong radial turbulent transport. The extent of the SOL width (λ_q) broadening depends strongly on outward turbulence spreading. The fluctuation energy intensity flux Γ_ε at the separatrix can be enhanced by increasing either pedestal E_r flow shear or local SOL pressure gradient. The λ_q is broadened as the fluctuation energy intensity flux Γ_ε at the last close flux surface (LCFS) increases. Local SOL $E \times B$ flow shear will restrain outward turbulence spreading and the associated heat flux width broadening. Operating in H-mode with small ELMs has the potential to solve two critical problems: reducing the ELM size and broadening the SOL width.

Keywords: plasma simulation, fusion plasma

1. Introduction

The high-confinement mode (H-mode), characterized by steep pressure gradients at the plasma edge and associated edge localized modes (ELMs), is the operational regime

† Email address for correspondence: li55@llnl.gov

foreseen for future fusion devices (Wagner *et al.* 1982; Mukhovatov *et al.* 2003; Shimada *et al.* 2007). However, type-I ELMs, characterized by a low repetition frequency and localized periodic collapse at the edge with large ELM size, are not expected to be tolerable due to the high heat and particle loads on plasma facing components in large-scale tokamaks, such as ITER (Mukhovatov *et al.* 2003; Loarte *et al.* 2007; Shimada *et al.* 2007) or future DEMONstration Power Plants (Riccardi *et al.* 2011; Eich *et al.* 2017). Simultaneous control of large ELMs and divertor heat loads in an H-mode plasma are crucial for steady-state operation of a tokamak fusion reactor. Recently, experiments showed that H-mode plasma regimes with small/grassy ELMs offer a potential solution for core-edge-integration to future tokamak reactors (Viezzler *et al.* 2023). In addition, DIII-D and ASDEX Upgrade experiments showed that the heat flux width is broadened with quasi-continuous particle and power exhaust to the divertors, and the peak divertor heat flux is much smaller for small/grassy ELMs (Nazikian *et al.* 2018; Xu 2020; Faitsch *et al.* 2021).

The exploration of small/grassy ELM regimes compatible with favourable energy confinement has intensively been conducted in many devices. A grassy ELM regime was found in JT-60U, which was compatible with high energy confinement in a carbon wall at a low pedestal collisionality $\nu^* \sim 0.29 - 0.72$ (Oyama *et al.* 2007). The grassy ELMs are characterized by a high repetition frequency and localized periodic collapse at the edge with small ELM size. The energy loss due to the grassy ELMs is estimated to be smaller than 1% of the pedestal stored energy. In NSTX, a small ELM regime (type-V ELM) was observed in discharges with boron wall conditioning at high ν^* (Maingi *et al.* 2005). EAST observed a grassy ELM regime in a metal wall at high density/collisionality ν^* (Xu *et al.* 2019a). A wide pedestal with a low pedestal density gradient is an essential condition for access to the grassy ELM regime, in addition to high q_{95} or high poloidal magnetic field B_p (Li *et al.* 2022a; Xu 2022). In AUG, the type-II ELM regime, where high confinement and small ELMs occur simultaneously, was achieved with high SOL density (Stober *et al.* 2001; Wolfrum *et al.* 2011). The quasi-continuous exhaust (QCE) regime was observed at the pedestal foot in the case with high separatrix density by gas fuelling (Harrer *et al.* 2018, 2022). The power fall-off length in the QCE regime measured with the infrared diagnostic in the divertor is increased by a factor of 4, when compared with the scaling for the inter-ELM power exhaust profile width (Faitsch *et al.* 2021). In JET, a Baseline Small ELM (BSE) regime has been found, where simultaneous access to small ELMs, high confinement and high D–D fusion rate were achieved without core impurity accumulation (Garcia *et al.* 2022).

To understand the underlying physics of these small/grassy ELM regimes, both theory and simulations are performed for different tokamak devices. Stability analysis for the JT-60U grassy ELM shows that short wavelength (high toroidal mode numbers) ballooning modes can play an important role in the stability of a grassy ELM. Low plasma ellipticity is preferable to realize a grassy ELM plasma, due to destabilization of the ballooning mode (Aiba & Oyama 2012). Linear edge stability analysis has shown that the pedestal in the BSE plasmas for JET is not limited by PB modes, indicating that mechanisms, other than ideal MHD, are responsible for the onset of such ELMs (Garcia *et al.* 2022). The underlying physics for such small ELMs in JET is still not clear and needs further investigation. JOREK simulations for ASDEX Upgrade with high density have successfully reproduced several key observations from the small ELM regime. These simulations suggest that the small ELMs may be driven by resistive peeling-ballooning modes, which exhibit strong localization near the separatrix (Cathey *et al.* 2022). BOUT++ nonlinear simulations for EAST indicate that small ELM crashes are accompanied by the upward movement of the peeling boundary induced by an initial

radially localized collapse in the pedestal, which stops the growth of instabilities (Xu *et al.* 2019a). The linear and nonlinear simulations for a long-pulse, high- q_{95} , high- B_p grassy ELM shows that the ELM crash is triggered by low- n peeling modes, and fluctuations are generated at the peak pressure gradient position and then radially spread outward into the scrape-off-layer (SOL) (Li *et al.* 2022b). The divertor heat flux width is ~ 2 times larger than that estimated by the ITPA multi-machines scaling law, due to strong turbulent transport (Li *et al.* 2022b). The pedestal density/collisionality and width scans for EAST indicate that small ELMs can be triggered by marginally unstable modes. These modes include low- n peeling modes, high- n ballooning modes, intermediate- n peeling-ballooning modes or a local ballooning instability in the pedestal foot, particularly in the presence of a larger separatrix density gradient (Li *et al.* 2022a). The size of the ELM, whether small or large, strongly depends on the inward avalanching and turbulence spreading from the linearly unstable zone to the stable zone during the nonlinear saturation phase (Li *et al.* 2022a). In the small/grassy ELM regime, the SOL turbulent thermal diffusivity increases due to larger turbulent fluxes being ejected from the pedestal into the SOL, resulting in a broadening of the SOL width (Li *et al.* 2019; Xu *et al.* 2019b; Li *et al.* 2020). Therefore, considering tokamak operational regimes with small ELMs may offer a potential solution to address the challenge of managing large transient heat loads in fusion reactors. However, several key aspects of the underlying physics in the small ELM regime remain unclear. Questions persist regarding how to control the inward penetration and outward spreading phenomena, and how these processes influence the size of ELMs and the width of the SOL. Further investigation is crucial to understand the impact of turbulence spreading on the evolution of edge profiles and SOL width.

To investigate the impact of turbulence spreading on pedestal energy loss (ELM size) and heat flux width broadening in the small ELM regime, we conducted BOUT++ (Dudson *et al.* 2009) turbulence simulations based on EAST experimental discharges, with variation in edge turbulence transport by altering the E_r and SOL profiles. The remainder of this paper is organized as follows. The BOUT++ six-field, two-fluid physics model (Xia, Xu & Xi 2013) and detailed simulation settings are introduced in § 2. The characteristics of avalanche and turbulence spreading phenomena in large and small ELMs are described in § 3. In § 4, the impact of E_r on the turbulence spreading and the associated ELM size is investigated. The impact of SOL profiles on edge fluctuations and turbulence spreading is studied in § 5. The impact of the turbulence spreading on heat flux width in the small ELM regime is presented in § 6. Finally, § 7 gives the conclusions and discussions.

2. Physics models and simulation settings

In our simulations, the electromagnetic six-field, two-fluid model within the BOUT++ framework has been used to simulate the edge turbulent transport and divertor power deposition in EAST discharges. The perturbations of vorticity ϖ , ion density n_i , ion and electron temperature T_i and T_e , ion parallel velocity $V_{\parallel i}$, and parallel magnetic vector potential A_{\parallel} are evolved to understand the ELM dynamics (Xia *et al.* 2013). This model is based on the full set of Braginskii equations, which considers both ideal MHD and non-ideal physics effects, such as the stability of peeling-ballooning modes, ion diamagnetic effects, resistivity, hyper-resistivity, the first order ion finite Larmor radius effect due to the gyro-viscous stress tensor, parallel thermal conduction, Hall effects, toroidal compressibility, electron-ion friction, etc. In the simulations, the Spitzer resistivity with Zeff correction is used and the viscosity is spatially constant. Quasi-neutral condition is assumed. Sheath boundary conditions are included by assuming that the ion velocity matches the sound speed at the sheath boundary: $V_{\parallel i} = C_s = \sqrt{k_B(T_e + T_i)/m_i}$.

The sheath heat fluxes are

$$q_{se} = -\chi_{\parallel e}^{\text{eff}} \partial_{\parallel} T_e = \gamma_e n_e T_e C_s, \quad (2.1)$$

$$q_{si} = -\chi_{\parallel i}^{\text{eff}} \partial_{\parallel} T_i = \gamma_i n_i T_i C_s, \quad (2.2)$$

where γ_e and γ_i are electron and ion sheath heat transmission factors, respectively. The temperature gradient is set by using the sheath heat flux divided by the parallel conductivity. Ion density and vorticity are set as the Neumann boundary condition in front of the target. In the radial direction, the Neumann boundary condition is applied on inner radial boundary surfaces while the Dirichlet boundary condition is used for the outer radial boundary surfaces for all the variables. For the pedestal region inside the LCFS, twist-shift periodic boundary conditions are set in the y direction along the magnetic field line and periodic boundary condition is used in the binormal direction. More detailed settings can be found in previous papers (Xia *et al.* 2013; Xia & Xu 2015). The flux-limiting parallel thermal conductivities (Malone, Mccrory & Morse 1975) are used to approximate the kinetic correction of parallel transport for a transition from collisionless to collisional regimes. In the simulations, we initiate the process with small perturbations characterized by a broad spectrum and random phases. These perturbations receive their free energy from plasma gradients, leading to the development of linear instabilities. As these perturbations progress through the linear phase and grow to significant amplitudes, the influence of nonlinear physics becomes increasingly dominant, marking the transition into the nonlinear saturation phase. Consequently, our simulations encompass both linear and nonlinear phases. During the linear phase, it is possible to meticulously investigate the underlying sources of instability drivers, such as the ballooning mode, peeling mode, drift-Alfvén mode, and more. However, during the nonlinear phase, we can delve into the characteristics of turbulence phenomena.

In this paper, two EAST discharges of small/grassy ELMs with different poloidal magnetic field are studied. These are shot #103745 with lower-single null divertor configuration (Li *et al.* 2022a) and high poloidal magnetic field B_p and #090949 with upper-single null divertor configuration (Li *et al.* 2022b) and low B_p . These two shots are simulated to investigate the impact of turbulence spreading on the ELM size and divertor heat flux width. For shot #103745, the small ELM is triggered by the marginal intermediate- n peeling-ballooning instability (Li *et al.* 2022a). For shot #090949, the small ELM is triggered by the low- n peeling mode (Li *et al.* 2022b). The simulations are radially global with both edge and SOL regions, which range from normalized poloidal flux $\psi_n = 0.75$ to $\psi_n = 1.05$ for shot #103745 and from $\psi_n = 0.8$ to $\psi_n = 1.1$ for shot #090949. The spatial resolution of the grid generated from the magnetic equilibrium file (kinetic EFIT g-file) is 260 radial grid points and 64 poloidal grid points. In the z -direction, 16 points are used for linear simulations and 64 points for nonlinear simulations. As for previous studies (Li *et al.* 2022a,b), the initial plasma profiles for these two discharges used in BOUT++ simulations are taken from fits of a modified hyperbolic tanh function (Groebner & Osborne 1998) to experimental data, mapped onto a radial coordinate of normalized poloidal magnetic flux with the SOL region, as shown by figure 1. However, due to the diagnostics limitation, the experimental data in the SOL sometime are not available. Therefore, we usually assume a flat or a small gradient profile from separatrix to outer boundary. To investigate the effect of SOL profiles on the edge turbulence transport and heat flux width, comparisons between flat and steep SOL profiles are presented in § 5, for shot #103745. In general, in our simulations, there is no radial electric field (E_r) profile provided from the experimental measurements. Therefore, E_r is calculated from force balance with the ion pressure P_{i0} without net flow, $E_r = 1/(n_0 Z_i e) \nabla P_{i0}$. This so-called

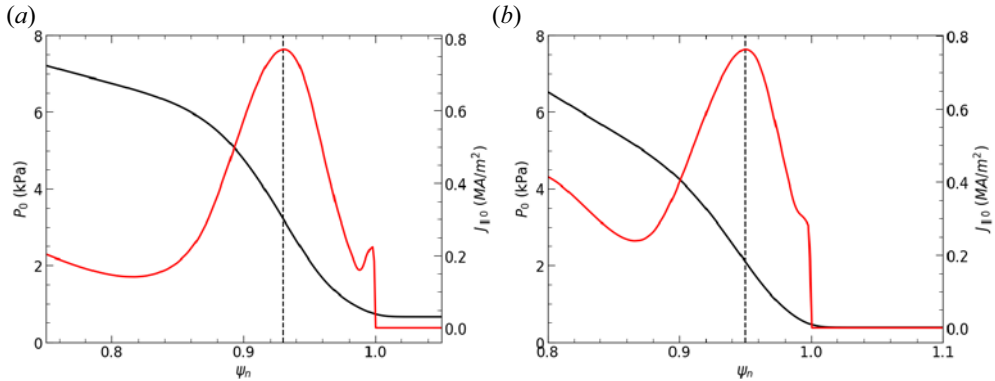


FIGURE 1. Initial profiles of total pressure (black) and parallel current (red) for shot (a) #103745 and (b) #090949. Here the dashed curves are at the location of peak total pressure gradient with $\psi_n = 0.93$ for shot #103745 and $\psi_n = 0.949$ for shot #090949.

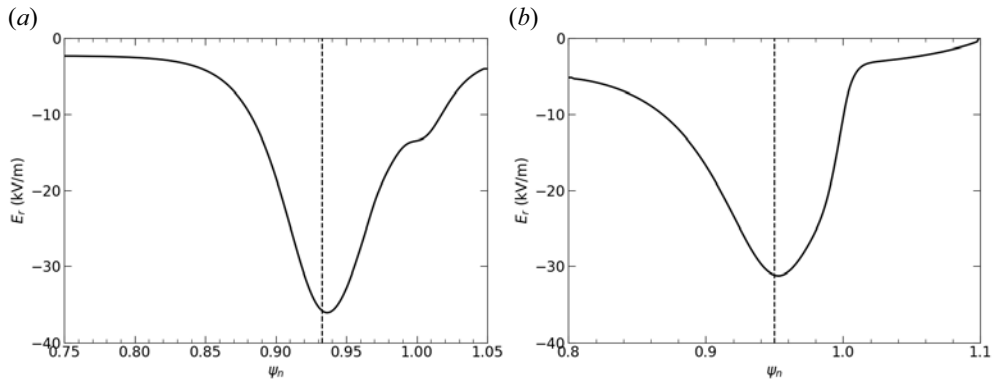


FIGURE 2. Radial electric field at outer midplane (OMP) for shot (a) #103745 and (b) #090949.

diamagnetic E_r is shown in figure 2. To study the impact of the E_r profile on the edge turbulence and divertor heat flux width, both linear and nonlinear simulations for the pedestal E_r scan are performed for shot #103745 in § 4.1. To study the effect of SOL $E \times B$ shear on the divertor heat flux width, two nonlinear simulations are compared for different SOL E_r profiles in § 4.2 for shot #090949. In this section, the two-dimensional (2-D) E_r profile is self-consistently calculated by the BOUT++ transport model (Li *et al.* 2018) with sheath boundary conditions on the divertor plates.

3. Characteristics of avalanche and turbulence spreading phenomena in large and small ELMs

Avalanche is originally used to describe a mass of snow, rock and/or ice falling down a mountain or incline, such as a snow avalanche. Turbulence spreading is typically used to describe the decoupling of local turbulence intensity or turbulent diffusivity from the local profile gradient. Both result in a deviation from local transport models. Here we report the non-local transport characteristics of the avalanches and turbulence spreading (Hahn & Diamond 2018) generated during the collapse of a pedestal transport barrier in large and small ELMs.

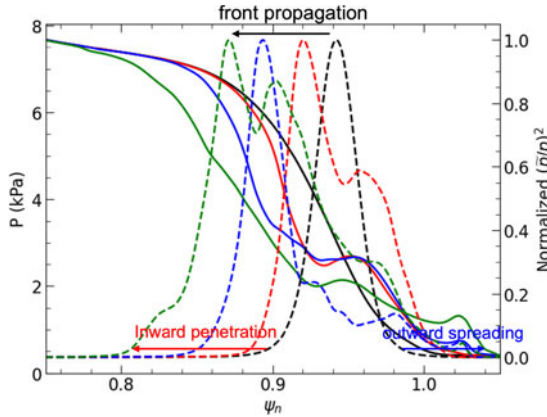


FIGURE 3. Radial total pressure profiles (solid curves) and normalized total pressure fluctuation intensity (dashed curves) at outer midplane for large ELM (shot #103751) at different time slices. Here the black curves are in the linear phase at $t = 60\tau_A$ with $\tau_A = 4.45 \times 10^{-7}$ s; the red, blue and green curves are in the nonlinear phase at $t = 80\tau_A$, $t = 150\tau_A$, $t = 310\tau_A$, respectively.

BOUT++ turbulence simulations (Li *et al.* 2022a) for a scan of pedestal density/collisionality and pedestal width show that the small ELM can be triggered near marginal instability in the pedestal by low- n peeling modes, intermediate- n peeling-ballooning modes or high- n ballooning modes. Whether the ELM is small or large strongly depends on the inward spreading of the edge fluctuation intensity. For large ELMs (shot #103751 for EAST) with diamagnetic E_r effect, the linear mode is very unstable with a large linear growth rate in the pedestal. A strong avalanche process occurs with multiple pedestal collapse events, as shown by figure 3. Here the solid curves show the total pressure profiles, while the dashed curves are normalized total pressure fluctuation intensity $(\tilde{p}/p)^2$ for large ELMs at different times during an ELM crash. In the linear phase, the mode first grows up at the peak gradient of total pressure, as shown by the black curves. Due to the large linear growth rate, the ELM is soon triggered and the profile crashes, as shown from the black to the red curve. The profile steepening shifts inward, resulting in linear instability there, and a second pedestal crash occurs. The pressure profile keeps crashing up to the pedestal top, as shown from the black to the red, blue and green curves, leading to fast front propagation (as black arrow indicates in figure 3) and deep inward penetration (as red arrow indicates in figure 3). The pedestal ELM energy loss for large ELM is much stronger with a large ELM size $\Delta W_{\text{ped}}/W_{\text{ped}} \gg 1\%$, where $\Delta W_{\text{ped}} = \int_{R_{\text{in}}}^{R_{\text{out}}} \oint dR d\theta (P_0 - P_\zeta)$ is the ELM energy loss and $W_{\text{ped}} = \frac{3}{2} P_{\text{ped}} V$ is the pedestal stored energy. The symbol P_0 is the equilibrium pressure; P_ζ is the toroidal average of perturbed pressure; R_{in} is at the inner boundary of simulated radial domain; R_{out} is at outer boundary and P_{ped} is the pedestal pressure. While for small ELMs with diamagnetic E_r effect, there is no clear front propagation for normalized pressure fluctuation intensity as shown in figure 4. Here the black curves are at linear phase (before the ELM crashes), while the red curves are the time average at the nonlinear phase for shot #103745. The time average in the nonlinear phase is for the red curves. The mode grows up first at the peak gradient position driven by the marginal unstable peeling-ballooning (P-B) modes. The small ELM is triggered on a long time scale due to the small linear growth rate. The fluctuation intensity saturates at a low level, in comparison with that of the large ELM. The pedestal profile relaxes below the P-B instability threshold after the initial ELM crash. Therefore,

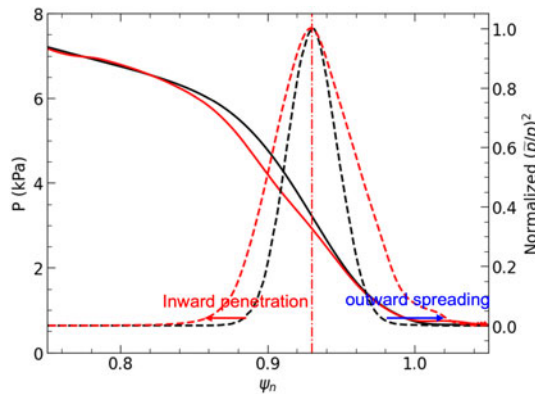


FIGURE 4. Radial total pressure profiles (solid curves) and normalized total pressure fluctuation intensity (dashed curves) at outer midplane in the linear (black curves) and the nonlinear phase (red curves) for small ELM (shot#103745).

the peak location of the mode will stay at the same location before and after the ELM crash, leading to small ELMs. The pedestal ELM energy loss fraction for small ELMs is much weaker than that of large ELMs. For the small ELM, the ELM size is $\sim 1\%$. Even though there is no clear front propagation and turbulence spreading is limited to within the pedestal, there is still inward penetration (as red arrow indicates in figure 4) for the small ELM.

Overall, these two special cases highlight the distinct characteristics of the large and small ELMs. (1) For larger ELMs, the triggering process occurs rapidly with a substantial linear growth rate, leading to a strong avalanche process and inward spreading during the nonlinear phase. These ELMs have a significant size with $\Delta W_{\text{ped}}/W_{\text{ped}} \gg 1\%$. (2) In contrast, small ELMs are triggered over a long time scale with a small linear growth rate. During the nonlinear phase, the peak of edge fluctuation intensity remains in the same radial location before and after the ELM crash. There is no clear front propagation, but instead, an inward penetration with small ELM size $\sim 1\%$. To further explore the impact of turbulence spreading on the pedestal dynamics and SOL radial transport, we conducted an E_r scan to study the inward spreading by changing the unstable modes, which reveals the transition from small to large ELMs. Section 4 will discuss in detail the E_r effect on the inward spreading. Additionally, regardless of the ELM size, we observed that during the ELM crash, energy is transported from the pedestal into the SOL. The phenomenon of strong outer fluctuation spreading occurs for both large and small ELMs, as shown by the blue arrows in figures 3 and 4. This enhances the radial turbulence transport, resulting in SOL width broadening. Section 6 will provide a more comprehensive analysis of the effect of outward turbulence spreading on the heat flux width.

It is worth noting that in these two simulations, we employed the diamagnetic E_r . However, edge E_r plays a crucial role in setting the edge turbulence transport. To investigate the influence of edge E_r on the turbulence spreading, we conducted an E_r scan in § 4 with two EAST small ELM discharges.

4. Impact of E_r on the edge dynamics

The edge $E \times B$ shear plays an important role in setting the edge turbulence transport. BOUT++ simulations have revealed that in the ELMy H-mode operation, the $E \times B$ shear flow can stabilize the high- n ballooning modes while inducing the Kelvin–Helmholtz

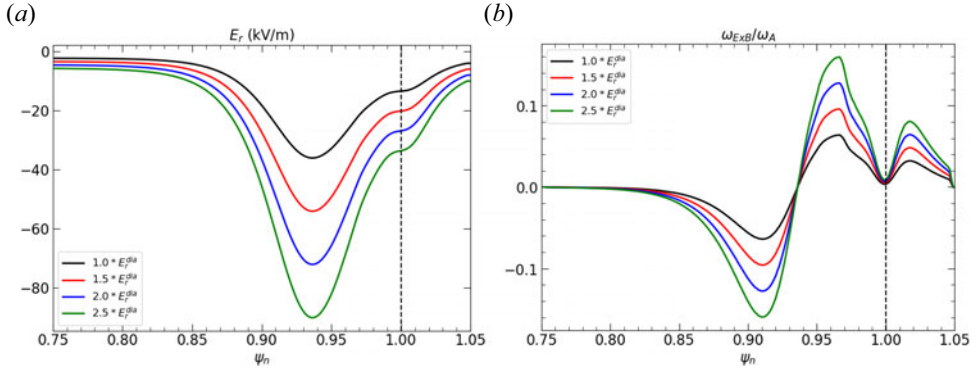


FIGURE 5. (a) Radial electric field (E_r) profiles and (b) normalized $E \times B$ shear rate at outer midplane for E_r scan with shot #103745.

instabilities through bootstrap current and rotational shear (Chen *et al.* 2017; Zhang, Guo & Diamond 2020). The stability of the pedestal plasmas and ELM dynamics are the outcome of the competition between these two effects. As discussed in § 3, the ELM size strongly depends on the inward spreading of edge turbulence. To study the impact of inward spreading on the ELM size and understand the transition from small to large ELMs, we conducted a series of BOUT++ nonlinear simulations with different E_r profiles. Section 4.1 presents the results of a pedestal E_r scan, focusing on the impact of turbulence spreading on ELM size. Furthermore, in § 4.2, we examine the impact of SOL $E \times B$ shear on the turbulence spreading. These simulations and analysis contribute to a deeper understanding of the underlying mechanisms driving the behaviour of ELM dynamics.

4.1. Edge E_r scan for small ELMs

According to the radial force balance, the E_r can be calculated by $E_r = E_r^{\text{dia}} + E_r^{V \times B}$. Here E_r^{dia} represents the diamagnetic component given by $E_r^{\text{dia}} = \nabla P_{i0}/n_0 Z_i e$ and $E_r^{V \times B}$ corresponds to the ion flow component, $E_r^{V \times B} = V \times B$. Additionally, P_{i0} is the ion pressure and Z_i is the charge number. Consequently, the pedestal $E \times B$ flow shear can be altered by modulating either the ion pressure profile or the toroidal plasma flow profile. In general, the pressure profile serves a dual role: (1) its gradient can drive edge MHD modes; and (2) its curvature can induce an $E \times B$ shear, which suppresses the underlying instabilities. While the pressure profile remains fixed for a given equilibrium from experiments, the pedestal E_r can be modified by toroidal plasma rotation, which can in turn modulate the $E \times B$ shearing profile without altering the pressure gradient. Therefore, with a given equilibrium from experiments, the pressure profile keeps constant. In our simulations, to modify the $E \times B$ shearing profile, we perform an E_r scan by multiplying the diamagnetic E_r^{dia} by a factor 1.0×, 1.5×, 2×, 2.5×, while keeping the pressure profile fixed for EAST shot #103745, as shown by figure 5(a). The black curve is the diamagnetic E_r^{dia} , determined by the pressure gradient and density profile. Essentially, the E_r scan is equivalent to the plasma flow V or $E_r^{V \times B}$ scan with varying flow profiles, generating the same profiles as the diamagnetic E_r , but with varying magnitudes. We label these four cases as E_r 1.0BLACK, E_r 1.5RED, E_r 2.0BLUE, E_r 2.5GREEN, respectively, corresponding to $E_r^{V \times B} = 0$, $E_r^{V \times B} = 0.5E_r^{\text{dia}}$, $E_r^{V \times B} = 1.0E_r^{\text{dia}}$, $E_r^{V \times B} = 1.5E_r^{\text{dia}}$. Furthermore, the corresponding $E \times B$ shearing rate $\omega_{E \times B}$ is calculated by using the expression $\omega_{E \times B} = ((RB_p)^2/B)(\partial/\partial\varphi)(E_r/RB_p)$, as shown by figure 5(b). The $E \times B$ shearing rate increases as the E_r well deepens.

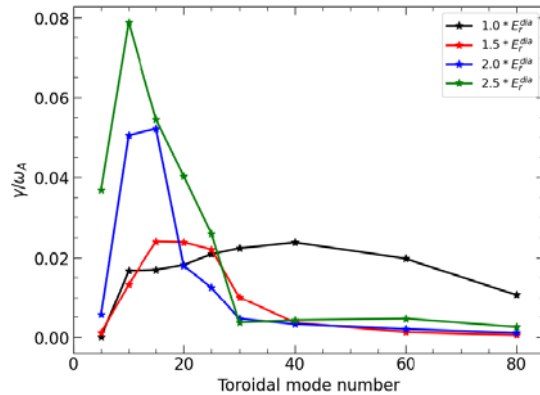


FIGURE 6. Linear growth rate versus toroidal mode number with different E_r .

To gain insights into the dominant modes under different E_r conditions, we conduct linear simulations by turning off the nonlinear terms in the equations. The linear simulations initiate from small random perturbations. Figure 6 shows the linear growth rate versus toroidal mode number n for the E_r scan. For the case with the diamagnetic E_r , represented by the black curve in figure 6, the pedestal exhibits marginally instability attributed to the peeling-ballooning mode with $n \sim 40$. However, for the case E_r 1.5RED scenario, the high- n modes are stabilized, whereas the low- n modes become destabilized. Consequently, the dominant modes shift from $n \sim 40$ to $n \sim 15$ – 25 while the mode spectrum narrowed, the largest linear growth rate has almost no change. As we further deepen the E_r , the low- n peeling modes become more sensitive to E_r and are strongly destabilized by its influence. Consequently, the dominant mode shifts to the low- n peeling modes, leading to a narrow mode spectrum and a significant increase in the linear growth rate. Particularly, for the case E_r 2.5GREEN, a large crash is observed compared with the other cases. The results of these linear simulations, indicating that the stabilization of high- n modes and destabilization of low- n modes by strong $E \times B$ flow shear, are in excellent agreement with previous BOUT++ work conducted in a circular geometry, as referenced by Chen *et al.* (2017) and Zhang *et al.* (2020). These findings contribute to our understanding of the behaviour of dominant modes under varying E_r shearing conditions.

To investigate the impact of the E_r effect on the edge turbulence spreading, the nonlinear turbulence simulations are conducted to capture the underlying physics of the ELM dynamics under different E_r profiles. The nonlinear simulations are performed using the same simulation settings as the linear simulations, with the only difference being activation of all nonlinear terms. To thoroughly explore both inward penetration and outward spreading, the radial simulation domain covers a range from normalized poloidal flux $\psi_n = 0.75$ to $\psi_n = 1.05$ for all these four cases, with the separatrix positioned at $\psi_n = 1.0$.

The pressure fluctuation intensity at the outer midplane is calculated in both the linear and nonlinear phase for these four cases from the simulations. Figure 7 presents the results, showing the normalized pressure fluctuation intensity at the outer midplane for linear (solid curves) and nonlinear phase (dashed curves) with different E_r . In all cases, the pedestal peak pressure gradient position is unstable to peeling-ballooning modes and the mode grows at that position observed in the linear phase (solid curves in figure 7). However, with deeper E_r wells, the linear growth rate increases and fluctuation intensity at the onset of ELM increases, leading to enhanced inward spreading. This trend is

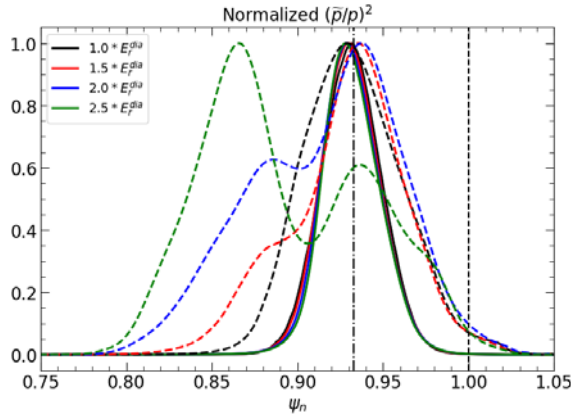


FIGURE 7. Normalized pressure fluctuation intensity at outer midplane in the linear (solid) and nonlinear phase (dashed) with different E_r .

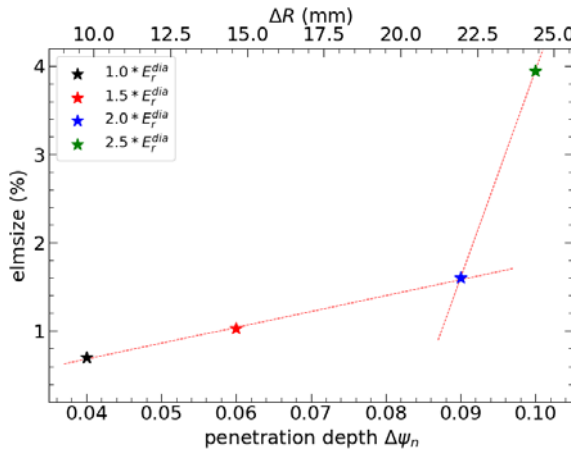


FIGURE 8. Inward turbulence spreading depth $\Delta\psi_n$ versus ELM size for E_r scan.

evident in the dashed curves in figure 7, showing increasing inward penetration. As inward penetration increases, the ELM size increases, as shown in figure 8. A comparison of the case $E_r2.5$ GREEN with the other three cases ($E_r1.0$ BLACK, $E_r1.5$ RED, $E_r2.0$ BLUE) reveals a notable shift inward of the mode’s peak location after the initial ELM crash. The strong avalanche process in the case $E_r2.5$ GREEN results in a large ELM crash. In contrast, for the cases from $E_r1.0$ to $E_r2.0$, although the inward turbulence spreading is enhanced due to deeper E_r wells induced by $E \times B$ net flow, the pedestal stabilizes linearly after the initial ELM crash. Consequently, the dominant mode in the nonlinear phase remains at the same location as in the linear phase, thus resulting in a small ELM.

To quantify the ELM size increasing due to inward penetration, the inward turbulence spreading depth $\Delta\psi_n$ is calculated by $\Delta\psi_n = \Delta_{\text{nonlinear}} - \Delta_{\text{linear}}$. Here Δ_{linear} is the penetration depth in the linear phase, while $\Delta_{\text{nonlinear}}$ is the penetration depth in the nonlinear phase. The penetration depth Δ is defined as the point where the front foot starts to decrease to 10^{-2} of the peak fluctuation intensity level, as defined by Li *et al.* (2022a). Figure 8 shows the relation between ELM size with inward turbulence spreading depth $\Delta\psi_n$. The ELM size exhibits a strong dependence on $\Delta\psi_n$. In the small ELM regime (black, red, blue stars in figure 8), the ELM size increases linearly with increasing $\Delta\psi_n$.

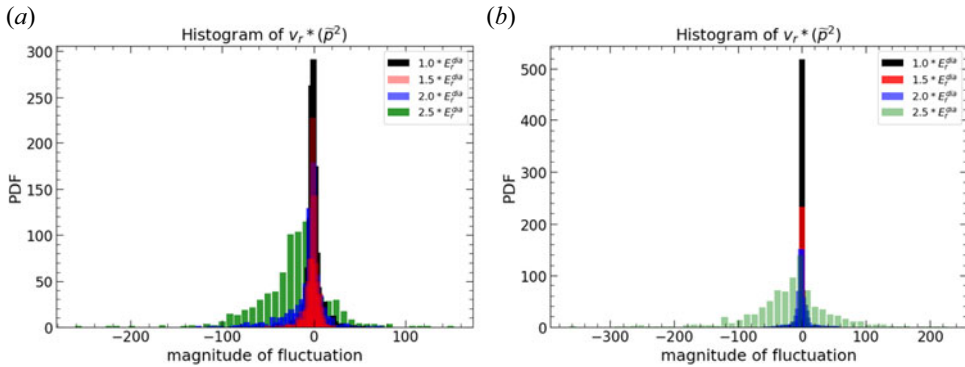


FIGURE 9. Probability distribution functions (p.d.f.s) of fluctuation energy flux $\Gamma_{\mathcal{E}} = V_r(\tilde{p}^2)$ in nonlinear phase (a) at peak pressure gradient position with $\psi_n = 0.93$ and (b) at pedestal top with $\psi_n = 0.85$.

For example, the ELM size increases by ~ 2.4 times from case $E_r 1.0$ to $E_r 2.0$, with $\Delta\psi_n$ increasing ~ 2.25 times. However, with the transition from small to large ELMs, the ELM size dramatically increases from $E_r 2.0$ to $E_r 2.5$ due to the stronger avalanche process. Our simulations demonstrate a positive correlation between ELM size and inward turbulence spreading depth, which corresponds to the extension of the area affected by the ELM, consistent with experimental measurements (Loarte *et al.* 2007; Kojima *et al.* 2009). The narrow radial extent of the density pedestal collapse due to grassy ELMs, as confirmed by fast density profile measurement using a lithium beam probe (LiBP) (Kojima *et al.* 2009), agrees with our simulation results. Further studies of avalanche and turbulence spreading will offer valuable insights for determining the ELM affected area and, consequently, aid in developing ELM control strategies.

To further investigate the impact of different E_r on inward and outward turbulence spreading, we analyse the probability distribution functions (p.d.f.s) of fluctuation energy flux $\Gamma_{\mathcal{E}} = V_r * (\tilde{p}^2)$ in the nonlinear phase at various radial locations (Li *et al.* 2023). Figure 9 illustrates the p.d.f.s at the peak pressure gradient position (figure 9a) and at the pedestal top with $\psi_n = 0.85$ (figure 9b). Positive values represent outward spreading, while the negative values indicate inward penetration. At the peak pressure gradient position, particularly near the inner edge of the E_r well, we observe that with deeper E_r wells, the $E \times B$ shear flow increases, driving strong linear instabilities, as shown in figure 6, and leading to strong avalanche and turbulence spreading, resulting in a large ELM crash. As a consequence, the p.d.f. becomes broadened on both sides, reflecting enhanced both inward and outward spreading, as shown by figure 9(a). Therefore, the inward penetration increases, as also demonstrated in figure 7. However, at $\psi_n = 0.85$, only the $E_r 2.5$ case displays a large tail in the p.d.f. of fluctuation energy flux $\Gamma_{\mathcal{E}}$, indicating strong inward and outward turbulent transport in the pedestal top, and leading to a large ELM. In contrast, the other three cases show only a small tail in the p.d.f., suggesting limited turbulence spreading, resulting in small ELMs.

In § 6, we will further investigate the relationship between outward turbulence spreading and the SOL width for different E_r profiles.

4.2. The impact of local SOL E_r on the turbulence spreading

In the pedestal region, E_r is primarily determined by radial force balance. However, in the SOL, E_r is strongly influenced by the SOL physics, such as the sheath boundary conditions.

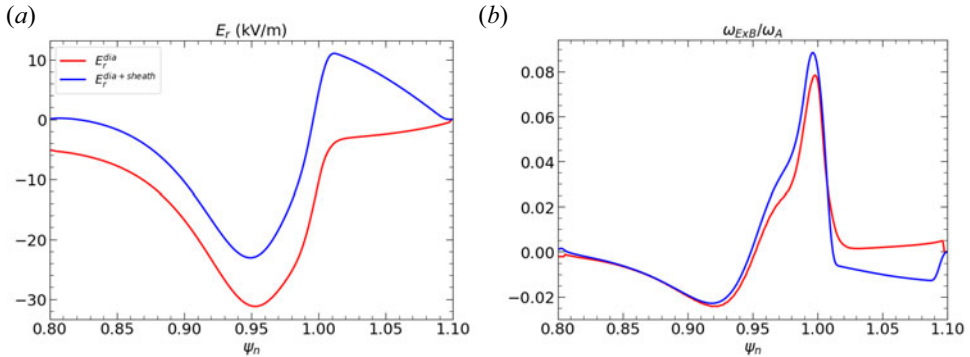


FIGURE 10. (a) Radial electric field profiles and (b) E_r shear rate at outer midplane with (blue) and without (red) sheath boundary conditions for shot #090949.

In § 4.1, we find a significant effect of pedestal E_r on both pedestal instability, and inward and outward turbulence spreading. However, the impact of SOL E_r on these processes remains less clear.

To explore the impact of local SOL E_r on turbulence spreading, E_r is self-consistently calculated using the BOUT++ 2-D transport module (Li *et al.* 2018). The simulation domain covers from the pedestal to the SOL. The BOUT++ 2-D transport module is distinct from the six-field, two-fluid turbulence module, and it includes the equations for ion density, ion momentum, and energy for both the electrons and ions based on Braginskii equations. By including cross-field drifts effects, the module yields steady-state 2-D plasma and E_r profiles across the separatrix. The plasma profiles inside the separatrix match experimentally measured profiles, while the E_r profiles inside the separatrix are consistent with those determined by radial force balance. Additional details about this module can be found in previous papers (Li *et al.* 2018, 2020).

In this study, the role of transport module is to establish the 2-D initial plasma profiles in the SOL and determine the E_r profile across the separatrix for turbulence simulations.

The edge E_r is determined by the force balance in the pedestal inside the separatrix and by the sheath boundary condition in the SOL. Figure 10 shows the E_r profile and the corresponding $E \times B$ shearing rate for EAST shot #090949. The red curve represents the diamagnetic E_r induced by the ion pressure gradient, while the blue curve represents the E_r simulated using the BOUT++ transport module. Notably, a large positive E_r is formed in the SOL due to the SOL physics and the sheath boundary conditions, as shown by the blue curve in figure 10(a). Inside the separatrix, E_r is mainly determined by the ion force balance. The ion viscous effect smoothly connects the pedestal E_r and the SOL E_r across the separatrix of the order of the ion gyro-radius scale, resulting in the identical E_r shape in the main pedestal region with diamagnetic E_r . Therefore, a large $E \times B$ shearing rate arises from the positive E_r in the SOL, with a marginal decrease observed in the inner edge of the E_r well, as shown in figure 10(b).

To compare the effect of local $E \times B$ flow shear on the edge turbulence spreading, we employ 2-D plasma and E_r profiles calculated from the BOUT++ transport module as inputs for BOUT++ six-field two-fluid turbulence nonlinear simulations.

The nonlinear simulations for shot #090949 with upper-single null divertor configuration show that the pedestal energy loss or the ELM size increases approximately 20% when using the E_r from simulations of the BOUT++ transport module, compared to the diamagnetic E_r . This is shown by the blue curve in figure 11(b). Moreover, when

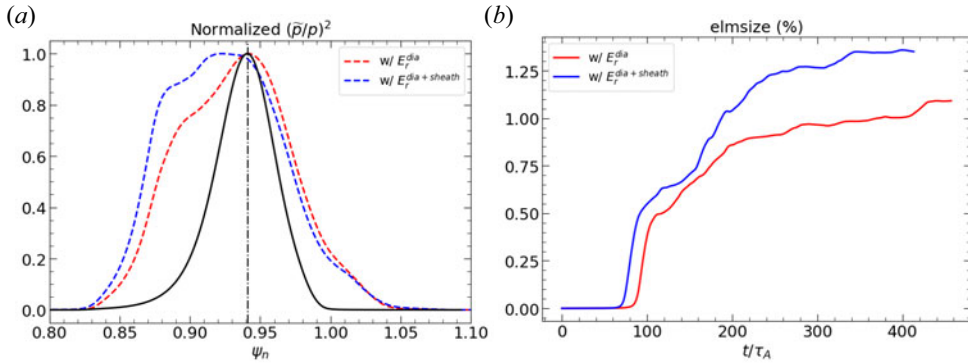


FIGURE 11. (a) Normalized pressure fluctuation intensity at outer midplane in the linear phase (black solid curve) and nonlinear phase (dashed curves) with different E_r ; (b) time evolution of 3-D energy loss fraction (ELM size) with different E_r . The red curves are with diamagnetic E_r while the blue curves are with E_r calculated by the BOUT++ transport module.

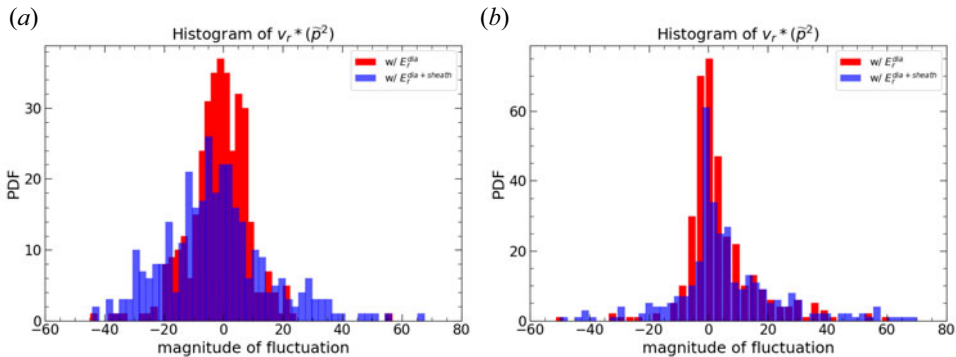


FIGURE 12. Probability distribution functions (p.d.f.s) of energy flux $V_r * (\tilde{p})^2$ in the nonlinear phase (a) at peak gradient of pressure with $\psi_n = 0.95$ and (b) at separatrix.

using the E_r from the simulation of transport module, the E_r inside the pedestal decreases, and the $E \times B$ shearing rate slightly decreases as well when compared to the diamagnetic E_r . The decrease in pedestal E_r destabilizes the pedestal and enhance the inward spreading of pedestal turbulence. As shown in figure 11(a), the inward penetration increases, leading to a large ELM size, as shown in figure 11(b). This stands in contrast to the findings in § 4.1, where the effect of E_r on the pedestal instability is opposite. Specifically, when the E_r is smaller than the diamagnetic E_r , a negative $E \times B$ shear flow is induced, resulting in the destabilizing effect on the pedestal instability. As pedestal E_r decreases to smaller than diamagnetic E_r , the linear growth rate increases, but with the same dominant mode, thereby inducing pedestal instability in both co- and counter direction of $E \times B$ shear flow. In summary, the pedestal E_r scan indicates that changing the pedestal E_r profile can enhance pedestal instability, consistent with experiment results, where strong turbulence can be triggered by NBI in both co- and counter direction (Burrell *et al.* 2005, 2009; Chen *et al.* 2016).

To compare the effect of local SOL E_r on inward and outward spreading at different radial location, the p.d.f.s of fluctuation energy flux $\Gamma_E = V_r * (\tilde{p})^2$ in nonlinear phase are calculated at the peak pressure gradient position and at the separatrix, as shown in figure 12. At the peak gradient location of the pedestal (figure 12a), the p.d.f. shift

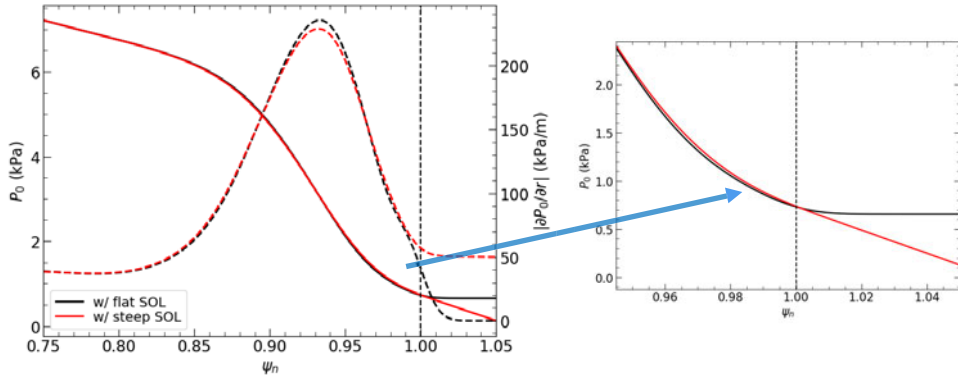


FIGURE 13. Radial profile of pressure (solid) and pressure gradient (dashed) with flat SOL (black) and steep SOL profiles (red).

towards to the negative value, indicating an increase in inward fluctuation energy flux and inward turbulence spreading. However, the positive fluctuation energy flux remains almost unchanged, and outward turbulence spreading is limited due to the strong $E \times B$ shearing rate at the pedestal bottom. Near the separatrix (figure 12b), both inward and outward energy flux decrease, resulting in smaller fluctuation, as shown by the dashed curves in figure 11(a). The blue dashed curve lies below the red dashed curve outside the peak pressure gradient location due to the suppression of turbulence spreading by the strong $E \times B$ shearing rate near the separatrix. Thus, the local SOL E_r can influence the turbulence spreading.

It is important to note that in these simulations, flat SOL profiles are assumed. The effect of local SOL profiles on the pedestal instability will be discussed in § 5, while the strong local $E \times B$ shearing rate's effect on outward turbulence spreading and the SOL width will be discussed in § 6.

5. Impact of SOL profiles on pedestal dynamics

In the previous sections, we analysed the transport of the fluctuation intensity from the pedestal to the SOL, effectively transferring it from unstable to stable regions, represented by fluctuation energy flux $\Gamma_{\mathcal{E}} = V_r * (\tilde{p})^2$. However, it has been observed in previous BOUT++ simulations that small ELMs can also be triggered by the local SOL instability with steep SOL profiles (Li *et al.* 2022a). To ensure a fair comparison and gain an understanding of the impact of this local instability on edge plasma dynamics, particularly associated with ELM size and SOL width, a local ballooning mode in the SOL is artificially excited by steepening the pressure profile in the SOL, as illustrated in the simulations for small ELM with shot #103745. To achieve this, we modify the density profile in the SOL while maintaining the same temperature profile to obtain the desired steep SOL pressure profile. This approach enables us to place the two physical phenomena on equal footing and provide deeper insights into their respective effects on the edge plasma dynamics.

In this section, two nonlinear simulations are performed: one with flat and the other with a monotonically decreasing (steep) SOL profiles, as shown in figure 13. The pressure profile with flat SOL is depicted by the black curve, while the red curve represents the profile with a monotonically decreasing (steep) SOL. For consistency, we use the diamagnetic E_r in these two cases. It is important to note that the case with flat SOL

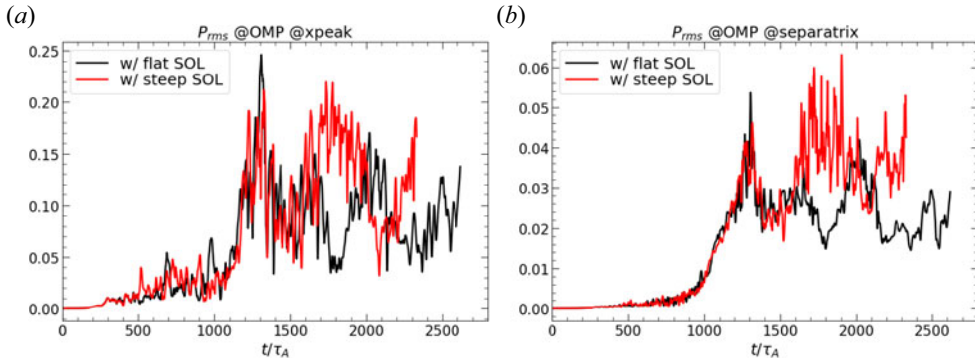


FIGURE 14. Time evolution of r.m.s. part of pressure at OMP for cases with flat SOL (black) and steep SOL profile (red): (a) at peak gradient location with $\psi_n \sim 0.93$ and (b) at separatrix.

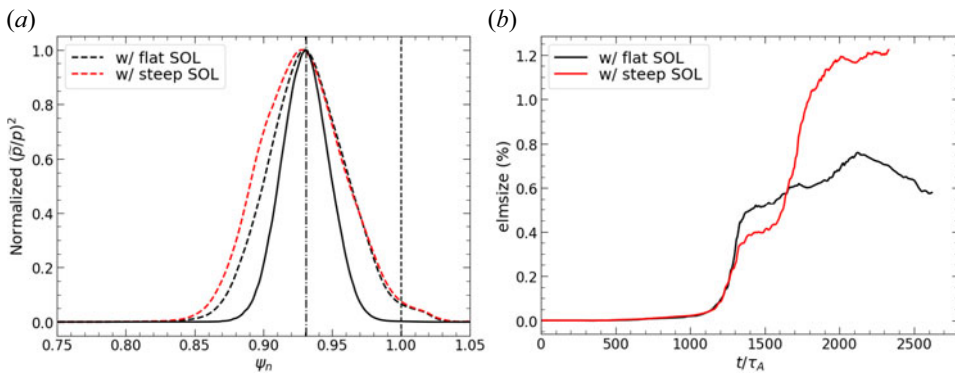


FIGURE 15. (a) Normalized pressure fluctuation intensity at outer midplane in the linear (solid) and the nonlinear phase (dashed); (b) time evolution of 3-D relative ELM size for cases with flat SOL (black) and steep SOL pressure profile (red).

profile is the same as the $E_r1.0BLACK$ case discussed in § 4, enabling a meaningful comparison. These two simulations are performed using the same nonlinear simulations setting to ensure accuracy and fairness in the comparison.

To investigate the impact of local instability on the generation of the turbulence at the edge, we calculate the time evolution of the pressure perturbation at different radial locations. Figure 14 shows the time evolution of the root-mean-square (r.m.s.) value of the pressure perturbation at the outer midplane, both at the location of peak gradient of pressure in figure 14(a) and at the separatrix in figure 14(b). In the linear phase, the dominant mode inside the pedestal, located at the peak pressure gradient for two cases, is driven by the ideal peeling-ballooning mode. Consequently, the pressure fluctuation levels are comparable between the two cases at this location. Near the separatrix, during the early nonlinear phase, the fluctuation levels are also comparable due to similar turbulent transport from the pedestal to the SOL. A small ELM is triggered with similar linear growth rate, resulting in comparable ELM size for two cases during this phase, as shown in figure 15(b). However, during the later nonlinear phase, a stronger pressure fluctuation is generated by the local SOL instability, specifically the ballooning mode induced by the steep SOL pressure gradient, as shown by figure 14(b). This enhanced radial turbulence

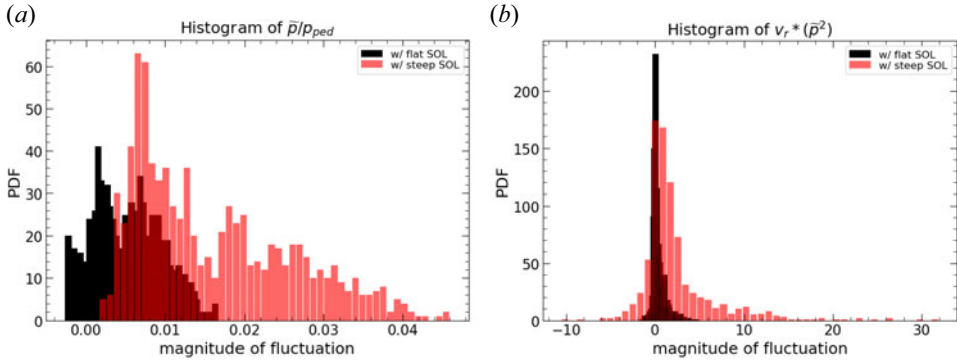


FIGURE 16. Probability distribution functions of (a) normalized pressure fluctuation \tilde{p}/p_{ped} and (b) energy flux $V_r * (\tilde{p})^2$ at pedestal bottom with $\psi_n = 0.99$ for cases with flat SOL (black) and steep SOL profile (red).

transport leads to a large pedestal crash, resulting in increased pedestal energy loss during this later nonlinear phase, as shown in figure 15(b).

As mentioned earlier, small ELMs can be triggered by a local instability at the pedestal bottom (Li *et al.* 2022a). The presence of a steep SOL pressure gradient drives a local ballooning instability in the SOL, leading to enhanced turbulence spreading. Now, we aim to explore how these local SOL profiles affect the inward spreading and the associated ELM size. For this analysis, we calculate the p.d.f.s of the normalized pressure fluctuation \tilde{p}/p_{ped} and fluctuation energy flux $\Gamma_{\mathcal{E}} = V_r * (\tilde{p})^2$ at the pedestal bottom during the nonlinear phase, as shown in figure 16. With the steep SOL profile, the p.d.f.s shift towards higher magnitude of pressure fluctuation, indicating a large outward spreading compared to the case with the flat SOL profile, as shown by figure 16(a). This finding is consistent with the r.m.s. part of the pressure near the separatrix, as shown in figure 14(b). Moreover, the p.d.f.s of fluctuation energy flux $\Gamma_{\mathcal{E}} = V_r * (\tilde{p})^2$ show that the steep SOL profiles promote enhanced inward and outward spreading, as shown in figure 16(b). Positive values represent outward energy flux transport, while negative values denote inward energy flux. With the transition from the flat SOL (black curve) to the steep SOL (red curve), the probability of the high-amplitude fluctuation energy flux events increases for both positive and negative energy flux. Consequently, both inward and outward spreading are enhanced by the steep SOL profile, leading to a larger inward penetration depth, as shown in figure 15(a). Here the solid curve represents the radial profile of normalized pressure fluctuation intensity at the outer midplane in the linear phase, while the dashed curves correspond to the nonlinear phase.

In the presence of the steep SOL profile, the inward mixing penetration broadens, resulting in a larger ELM size, as shown in figure 15(b). Additionally, the enhanced outward turbulence spreading due to the local instability can broaden the divertor heat flux width. Further details regarding the outward turbulence spreading versus the SOL width will be discussed in § 6.

6. Impact of turbulence spreading on the divertor heat flux width

In the small ELM regime, a strong turbulence spreading occurs both inward and outward, in contrast to the ELM-free regime. The inward spreading leads to an increase of the ELM size, while the outward spreading facilitates strong radial turbulent transport in the SOL region, even when the SOL is locally stable. To investigate the impact of outward

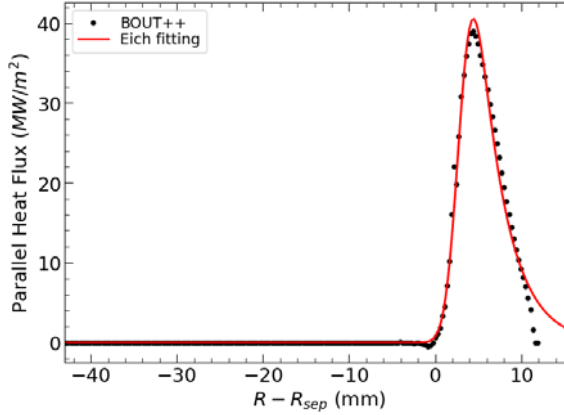


FIGURE 17. Parallel heat flux on the outer divertor with the diamagnetic E_r for shot #103745; the black points are from BOUT++ simulations and the red curve is a fit to the profile using the Eich fitting formula (Eich *et al.* 2011).

turbulence spreading on the divertor heat flux width, the parallel heat flux is calculated on the outer divertor target for different E_r and SOL profiles, as described in §§ 4 and 5. The heat flux width is calculated using the Eich fitting formula (Eich *et al.* 2011; 2013), represented by the expression:

$$q(\bar{s}) = \frac{q_0}{2} \cdot \exp\left(\left(\frac{S}{2\lambda_q}\right)^2 - \frac{\bar{s}}{\lambda_q \cdot f_x}\right) \cdot \operatorname{erfc}\left(\frac{S}{2\lambda_q} - \frac{\bar{s}}{S \cdot f_x}\right), \quad (6.1)$$

and $\bar{s} = (R - R_{\text{sep}}) \cdot f_x$. Here R is the major radius with R_{sep} denoting the separatrix position at the outer midplane and f_x is the effective magnetic flux expansion from the outer midplane to the divertor. Using this fitting formula, the width λ_q and the divertor power spreading parameter S can be obtained. Figure 17 presents an example of the fitting for the BOUT++ simulation data for the small ELM case with shot #103745 (E_r , 1.0BLACK in § 4.1). The black points show the BOUT++ simulation data for the parallel heat flux on the outer divertor target with the diamagnetic E_r^{dia} . The red curve represents the fit to the simulation data using the fitting formula with $\lambda_q^{\text{fit}} = 3.24$ mm and $S = 1.85$ mm. To account for the larger spreading factor S dominating over λ_q , we use the integral power decay length λ_{int} in the paper (Eich *et al.* 2011). For this small ELM case, the integral power decay length is $\lambda_{\text{int}} = 6.27$ mm. The integral power decay length λ_{int} is significantly larger than λ_q due to the peak heat flux location shifts outward from separatrix with small ELMs. The ITPA multi-machine scaling law provides $\lambda_q^{\text{Eich}} \sim 4.08$ mm calculated by the formula (Eich *et al.* 2011) $\lambda_q^{\text{Eich}} = 0.63 \times B_{\text{pol,MP}}^{-1.19}$. The width calculated by Goldston heuristic drift (HD) model with the formula (Goldston 2012) $\lambda_q^{\text{HD}} = (4a/\bar{Z}eB_pR)(\bar{A}m_p T_{\text{sep}}/(1 + \bar{Z}))^{1/2}$ is $\lambda_q^{\text{HD}} \sim 6.90$ mm. Here B_p is the poloidally averaged value of poloidal magnetic field near the separatrix. Since the simulation and ITPA scaling law results are mapped to the outer midplane, the HD model gives $\lambda_q^{\text{HD*}} \sim 3.68$ mm mapping to the outer midplane. The integral power decay length λ_{int} from BOUT++ simulation is larger than the predictions of λ_q^{Eich} and $\lambda_q^{\text{HD*}}$ due to large radial turbulent transport with small ELMs. Notably, in BOUT++ turbulence simulation, we just simulate the ELM crash process, but not the profile recovery process. There are no ELM cycles. However, for the small ELMs, the variation of peak heat flux is <50 % with quasi-continuous power exhaust to the divertors

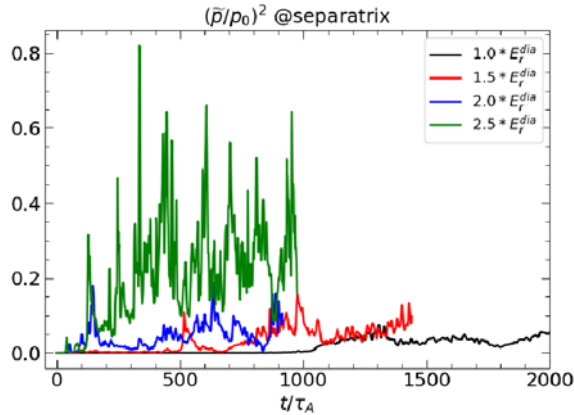


FIGURE 18. Time evolution of fluctuation intensity $(\tilde{p}/p_0)^2$ at outer midplane near the separatrix with different radial electric field profile.

and high ELM frequency. The heat flux width calculated based on the peak heat flux time point is close to the average over multiple ELM cycles for small ELMs.

To investigate the relation between the turbulence spreading and divertor heat flux width, we conducted a series of simulations with different levels of the edge fluctuation by varying the radial electric field and SOL profile, as discussed in the previous sections. The spatio-temporal evolution of the fluctuation intensity $(\tilde{p}/p_0)^2$ at the LCFS serves a good indicator of turbulence spreading. As demonstrated in § 4.1, a deeper E_r well leads to the increased pedestal energy loss, resulting in stronger energy transport from the pedestal to the SOL. Figure 18 shows the time evolution the fluctuation intensity $(\tilde{p}/p_0)^2$ at the LCFS of the outer midplane for different cases: E_r 1.0BLACK (black curve), E_r 1.5RED (red curve), E_r 2.0BLUE (blue curve) and E_r 2.5GREEN (green curve). As the E_r well deepens, the fluctuation intensity at the LCFs increases, and the time-averaged fluctuation level during the nonlinear phase also increases. For cases with small ELMs (E_r 1.0BLACK, E_r 1.5RED, E_r 2.0BLUE), the fluctuation level is much smaller than in the case with large ELMs (E_r 2.5GREEN) due to the larger pedestal crash experienced in the latter. In summary, the analysis of the fluctuation intensity at the LCFS help us better understand the relationship between turbulence spreading and the divertor heat flux width λ_q , showing that a deeper E_r well will lead to enhanced turbulence spreading and higher fluctuation levels. Additionally, small ELM cases exhibit significantly lower fluctuation levels compared with large ELM cases due to differences in the pedestal crash behaviour.

As we mentioned in the previous section, the extent of both inward and outward turbulence spreading is heavily influenced by the magnitude of fluctuation energy flux. To investigate the correlation between turbulence spreading and divertor heat flux width, we introduce the fluctuation energy density flux $\Gamma_\varepsilon = c_s^2 \tilde{V}_r (\tilde{p}/p_0)^2$ at the last closed flux surface. This measurement quantifies the turbulence spreading from the pedestal to the SOL. Here c_s represents the sound speed and \tilde{V}_r denotes the fluctuation in radial velocity. In the pedestal E_r scan, an increase in $E \times B$ flow results in a corresponding rise in edge fluctuation energy intensity flux, leading to a broadening of the divertor heat flux width, as shown by the data points in figure 19. The black, red and blue points represent small ELM, while the green point corresponds to a large ELM. The dashed black horizontal line represents the width based on the ITPA multi-machine scaling law. Consequently, as we transition from ELM-free to small and then to larger ELMs, the divertor heat flux width experiences significant broadening due to strong radial turbulence spreading from the

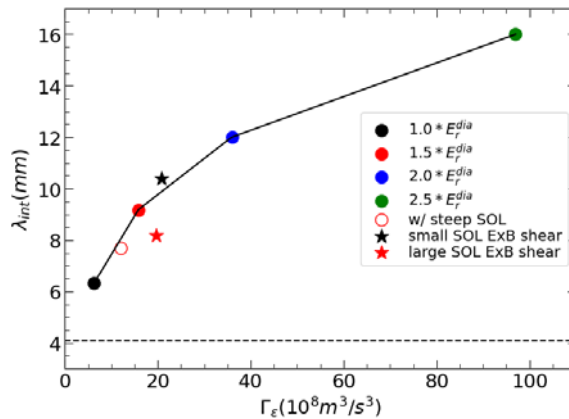


FIGURE 19. Divertor heat flux width λ_{int} versus fluctuation energy intensity flux Γ_{ε} .

pedestal to the SOL. Notably, DIII-D experiments using Resonant Magnetic Perturbations (RMPs) 3-D fields have also demonstrated that, from the inter-ELM phase to the grassy ELM phase (achieved by increasing RMP current), the width on the inner divertor target increases approximately two times with low RMP current and approximately four times with high RMP current. However, it is important to note that the peak divertor heat flux is much smaller compared to the case of type-I ELMs (Nazikian *et al.* 2018; Xu 2020). Nevertheless, due to the diagnostic limitations, further investigation is required to establish the relationship between turbulence and heat flux width from experimental data. In our simulations, we employ the heat flux profile at the end of a simulation to estimate the width for the large ELM.

Despite the significant broadening of heat flux width observed from small ELMs to large ELMs, it is essential to acknowledge that the pedestal relaxation is much stronger for large ELMs, resulting in a larger ELM size and higher peak heat flux. However, due to the large energy loss from pedestal to SOL for large ELMs, the peak heat flux deposited on the divertor is considerably larger compared to small ELMs, exceeding it by more than one order of magnitude. This poses a concern, particularly for ITER (Loarte *et al.* 2007; Eich *et al.* 2017), where such high heat flux with large ELMs is not tolerable for the materials, such as carbon and tungsten. However, for small ELMs, the ELM size is significantly smaller compared to that of large ELMs, yet allowing the heat flux width to be broadened with a decreasing peak heat flux. From the pedestal E_r scan, as discussed in § 4.1, it demonstrates that λ_{int} can be broadened up to $3 \times$ larger (blue point) than predicted by the multi-machine scaling law (dashed line in figure 19) and HD model with small ELMs. Here it should be noted that the comparison between λ_{int} and λ_q from ITPA scaling law may be not exactly equal. The integral power decay length λ_{int} in experimental devices is significantly larger than λ_q as the peak heat flux location shifts outward, which is related to the S parameter. Further investigation with the S effect is more relevant.

When comparing the impact of pedestal E_r on the divertor heat flux width with the effect of local SOL E_r shear, we observe a suppressing effect on the heat flux width. The divertor heat flux width decreases with strong local SOL $E \times B$ shear, as indicated by the stars in figure 19. The black star represents a case with small SOL $E \times B$ shear, while the red star corresponds to the case with strong SOL $E \times B$ shear. Two mechanisms are at play to reduce the heat flux width with strong local SOL $E \times B$ shear: (1) the $E \times B$ shear in the SOL suppresses turbulence spreading in that region, leading to reduced radial

transport; (2) the strong SOL E_r increases the parallel velocity induced by the $E \times B$ drift and reduces the parallel transport time, thus enhancing the parallel transport (Li *et al.* 2021). Additionally, as discussed in § 5, the local SOL instability can enhance outward turbulence spreading by increasing the SOL pressure gradient. The divertor heat flux width λ_{int} and fluctuation energy intensity flux Γ_ε with a steep SOL profile is also calculated, as shown by the red circle in figure 19. With a steep SOL profile, the fluctuation energy intensity flux increases, consequently broadening the heat flux width.

In table 1, we summarize the main results of our study. Both the E_r profiles and SOL profiles are found to play crucial roles in both inward and outward turbulence spreading in H-mode with small/grassy ELMs. Notably, the increase in inward spreading leads to a larger ELM size, while outward spreading can broaden the SOL width. These findings are consistent with the theory of turbulence spreading (Chu, Diamonds & Guo 2022). Figure 19 provides a comprehensive overview of the divertor heat flux width λ_{int} plotted against the fluctuation energy intensity flux Γ_ε for all the cases discussed in this paper. The results show that as the edge fluctuation energy intensity flux increases, the heat flux width can be significantly broadened. Particularly, in the small ELM regime, control of edge fluctuations, such as increasing pedestal $E \times B$ net flow, decreasing local SOL $E \times B$ shear or enhancing local SOL turbulence by steep SOL profiles, can lead to significant broadening of the divertor heat flux width λ_{int} . These findings offer promising possibilities for controlling and optimizing heat flux distribution in fusion reactors with both high confinement operations and tolerable divertor exhaust.

7. Summary and discussion

We conduct BOUT++ six-field two-fluid turbulence simulations to investigate the effects of turbulence spreading on the ELM size and the divertor heat flux width. The simulations focus on EAST discharges with small ELMs, specifically shot#103745 and shot #090949, and their evolution by varying the pedestal E_r , the SOL E_r and SOL profiles. The BOUT++ simulations show that the E_r profile and local SOL instability significantly influence the edge turbulence spreading and divertor heat flux width. To study the impact of E_r on the edge plasma dynamics, we perform a pedestal E_r scan for shot #103745 by multiplying the diamagnetic E_r^{dia} by factors $1.0\times$, $1.5\times$, $2\times$, $2.5\times$ while keeping the pressure profile fixed (§ 4.1). Essentially, the E_r scan is equivalent to the plasma flow V or $E_r^{V \times B}$ scan with specific flow profiles, generating the same profiles as the diamagnetic E_r , but with varying magnitudes. For investigating the local SOL $E \times B$ shear effects on SOL turbulence and divertor heat flux, we self-consistently simulate the edge E_r using the BOUT++ transport module in a radial domain across the separatrix and with sheath boundary conditions on the divertor plates for shot #090949 (§ 4.2). Additionally, we study the impact of the local SOL instability on both inward and outward turbulence spreading by steepening the SOL pressure profile for shot #103745 (§ 5). These comprehensive simulations shed light on the physics mechanisms controlling turbulence spreading and divertor heat flux, providing valuable insights for fusion plasma research and reactor design.

In BOUT++ linear simulations, we conduct a pedestal E_r scan for small ELMs (shot #103745) and observe the following trends. As the pedestal E_r well deepens, the high- n ballooning modes become stabilized, while the low- n peeling mode is destabilized. This shifts the dominant modes from high- n to low- n modes with a narrow mode spectrum and the maximum linear growth rate increases. Moving to the nonlinear simulations, we find that the fluctuation level increases, as the E_r well deepens, leading to an increased inward penetration toward the pedestal top and, consequently, an increased ELM size. However, these three cases remain within the small ELM regime, as no front propagation occurs.

| Control parameters | Key mechanism | Inward spreading | ELM size | Outward spreading | λ_{int} (figure 19) |
|----------------------------------------------------------|-------------------------------------------------------------|------------------------------------|-----------------------------------|-------------------|-----------------------------|
| Radial electric field (E_r) | | | | | |
| With diamagnetic E_r^{dia} | Stabilize pedestal high- n ballooning mode | Suppressed | Decrease | Suppressed | Narrowing |
| With sheath E_r : $E_r^{dia+sheath}$ (§ 4.2) | SOL turbulence spreading suppressed | Effect slightly enhanced | Effect slightly | Suppressed | Narrowing |
| With net flow: $E_r^{dia} + E_r^{V \times B}$ (§ 4.1) | Stabilize high- n ballooning mode | Enhanced | Increase | Enhanced | Broadening |
| | Destabilize low- n peeling mode | Inward penetration depth increases | Small ELM \rightarrow large ELM | | |
| | Narrow mode spectrum Increase maximum linear growth rate | | | | |
| SOL profiles | Steep SOL profiles (§ 5) | Enhanced | Increase \rightarrow Small ELM | Enhanced | Broadening |

TABLE 1. Radial electric field and local SOL instability effects on the ELM size and SOL width λ_q .

In the small ELMs, the pedestal relaxes into a linearly stable profile after the initial ELM crash. In contrast, when the E_r is further increased, such as in the case $E_r 2.5\text{GREEN}$, the fluctuation level significantly increases and the profile steepening shifts inward after the initial ELM crash at the peak pressure gradient position. As a result, the linear instability zone shifts inward, leading to a second pedestal crash. This continuous pressure profile crashing extends up to the pedestal top, triggering fast front propagation and deep inward penetration. We term this phenomenon an ‘avalanche process’, characterized by a rapid front propagation and the occurrence of the large ELMs. Therefore, the transition from small to large ELMs occurs by increasing inward turbulence spreading with the increasing pedestal $E \times B$ net flow. Additionally, the outward SOL spreading is enhanced due to the increased fluctuation level and turbulent transport from the pedestal to the SOL. In summary, the pedestal E_r scan reveals the following characteristics of turbulence spreading for ELMs.

- (1) For the large ELMs, the pedestal exhibits remarkable instability with a high linear growth rate. This leads to a strong avalanche process during the nonlinear phase, characterized by a robust inward penetration of the mixing zone. Consequently, the ELM size becomes significantly large, often with $\Delta W_{\text{ped}}/W_{\text{ped}} \gg 1\%$.
- (2) For the small ELMs, the pedestal approaches a state of near marginal stability. Following the initial ELM crash, the pedestal relaxes into a state of linear stability. While a distinct front propagation might not be evident, a prominent inward penetration is still observed. The ELM size is much smaller than that of the large ELMs. It is worth noting that the regime of ‘near marginal stability’ holds crucial significance here.

As the pedestal $E \times B$ shear flow increases, an intriguing pattern emerges: the high- n ballooning modes experience stabilization, while the low- n peeling modes undergo destabilization. This dual effect leads to an increase in the maximum linear growth rate and a narrowing of the mode spectrum. The process of enhanced inward turbulence spreading is triggered by increasing pedestal E_r . Remarkably, even within the small ELM regime, augmenting the inward penetration depth can lead to an increase in the ELM size. It is worth noting that the E_r scan performed in this study holds equivalence to the plasma flow V scan, characterized by specific flow profiles that generate the same profiles as the diamagnetic E_r , albeit with varying magnitudes. The practical implementation of this approach within an experimental setting necessitates further investigation.

- (3) In the course of ELM events, both strong inward and outward spreading phenomena are observed. The ELM size strongly depends on the extent of inward spreading. Within the small ELM regime, the ELM size exhibits an almost linear correlation with the depth of inward penetration. Moreover, the outward spreading amplifies the levels of fluctuation and the energy intensity flux Γ_ε at the LCFS, thereby enhancing turbulence transport from the pedestal to the SOL. This augmentation can lead to a broadening of the SOL width by approximately three times, in comparison to the ITPA multi-machine scaling law, prominently driven by strong outward turbulence spreading.

Furthermore, within the scope of this paper, an exploration of the impact of local SOL $E \times B$ shear and local SOL instability on turbulence spreading is undertaken. To attain a more realistic E_r profile that encompasses SOL physics, accounting for sheath boundary effects, the BOUT++ transport module is used to self-consistently simulate the E_r profile. Through comparisons with SOL $E \times B$ shear and those excluding it, it is evident that

local SOL $E \times B$ shear has a strong effect on the outward SOL turbulence spreading. This influence leads to a suppression of outward SOL turbulence spreading when a substantial local SOL $E \times B$ shear is present. BOUT++ nonlinear simulations are employed to investigate the effects of both flat and steep SOL profiles. These simulations reveal that local SOL instability is capable of driving both strong inward and outward turbulence spreading. Particularly under a steep SOL profile, a substantial inward energy flux is induced, leading to a heightened level of inward turbulence spreading. This augmentation subsequently contributes to an escalation in the size of ELMs.

In our BOUT++ simulations, we examined the behaviour of the divertor heat flux width λ_q , revealing its close association with the outward spread of edge fluctuation from the pedestal to the SOL within the small ELM regime. Notably, the increase in the divertor heat flux width λ_q corresponds to heightened levels of fluctuation energy intensity flux Γ_ε at the last closed flux surface, aligning well with turbulence spreading theory. As the pedestal E_r well deepens due to additional net flow (as described in §4.1), the spreading of pedestal turbulence is amplified. This enhanced transport from the pedestal to the SOL propels an increase in Γ_ε , thereby leading to a broader divertor heat flux width. However, it is important to note that the local SOL $E \times B$ shear plays a dual role. While it suppresses outward turbulence spreading, it simultaneously enhances the parallel transport within the SOL, resulting in a reduced heat flux width. Furthermore, the local SOL turbulence contributes to both inward and outward turbulence spreading, thereby leading to an increased fluctuation energy intensity flux Γ_ε . Overall, the divertor heat flux width λ_q undergoes significant broadening within small ELM regimes, as compared to the ELM-free regime, largely attributed to the strong radial turbulent transport. As the ELM size increases, the heat flux width increases. These are consistent with the experimental evidence of an increased ELM wetted area with ELM size (Eich *et al.* 2011, 2017).

This paper focuses on the simulation results concerning the characteristic of pedestal turbulence spreading within the ELM regimes and its impact on both ELM size and heat flux width. In pursuit of a more comprehensive understanding, additional comparisons with experimental data warrant deeper investigation. The following issues of significance include the following.

- (1) The E_r scan indicates that raising the pedestal E_r profile can significantly amplify pedestal instability, and the reduction of SOL E_r is linked to the broadening of the heat flux width. This suggests a potential pathway to transition into the small ELM regime through controlled adjustments of the E_r profile, possibly achieved by controlling toroidal rotation. Nevertheless, the question is: Can this conceptual approach feasibly translate into experimental implementation?
- (2) The size of ELMs finds its roots in the depth of inward turbulence spreading, closely linked to the area affected by the ELM, as discussed in experimental measurements. Further exploration through studies of avalanche and turbulence spreading could offer valuable insights into precisely determining the extent of the ELM-affected area and subsequently building strategies for ELM control. Further research is needed to control and predict these factors in experiments.
- (3) The fluctuation energy intensity flux Γ_ε is a critical parameter, effectively bridging the gap between pedestal physics and divertor heat flux width λ_q within the small ELM regime. It is noteworthy that λ_q increases correspondingly with an increase in fluctuation energy intensity flux Γ_ε at the LCFs. This relationship presents an opportunity for experimental measurement. However, the precise value of the optimal Γ_ε in the small ELM regime remains undetermined.

In conclusion, the potential of operating in H-mode with small ELMs offers a promising avenue for addressing two critical challenges: the reduction of ELM size and the expansion of the SOL width. However, the pathway to effectively controlling the parameters required to access this promising regime in experimental settings necessitates dedicated further research endeavours.

Acknowledgements

The authors thank Dr Z. Li, Dr H. Wang, Dr Q. Yang, and the BOUT++ team and the EAST experimental team for valuable discussions. This research used resources of the National Energy Research Scientific Computing Center, a DOE Office of Science User Facility supported by the Office of Science of the U.S. Department of Energy under Contract No. DE-AC02-05CH11231.

Editor Paolo Ricci thanks the referees for their advice in evaluating this article.

Declaration of interests

The authors report no conflict of interest.

Funding

This work was performed under the U.S. Department of Energy by Lawrence Livermore National Laboratory under Contract No. DE-AC52-07NA27344, LLNL-JRNL-843534 and by UCSD under Contract No. DE-FG02-04ER54738. This work also was supported by the SciDAC ABOUND Project, SCW1832 and by the Users with Excellence Program of Hefei Science Center, CAS under grant Nos. 2021HSC-UE014.

REFERENCES

- AIBA, N. & OYAMA, N. 2012 Numerical analysis of key factors for the appearance of grassy ELMs in Tokamak plasmas. *Nucl. Fusion* **52** (11), 114002.
- BURRELL, K.H., *et al.* 2005 Advances in understanding quiescent H-mode plasmas in DIII-D. *Phys. Plasmas* **12** (5), 056121.
- BURRELL, K.H., OSBORNE, T.H., SNYDER, P.B., WEST, W.P., FENSTERMACHER, M.E., GROEBNER, R.J., GOHIL, P., LEONARD, A.W. & SOLOMON, W.M. 2009 Quiescent H-mode plasmas with strong edge rotation in the cocurrent direction. *Phys. Rev. Lett.* **102** (15), 155003.
- CATHEY, A., HOELZL, M., HARRER, G., DUNNE, M.G., HUIJSMANS, G.T.A., LACKNER, K., PAMELA, S.J.P., WOLFRUM, E. & GÜNTER, S. 2022 MHD simulations of small ELMs at low triangularity in ASDEX Upgrade. *Plasma Phys. Control. Fusion* **64** (5), 054011.
- CHEN, X., *et al.* 2016 Rotational shear effects on edge harmonic oscillations in DIII-D quiescent H-mode discharges. *Nucl. Fusion* **56** (7), 076011.
- CHEN, J.G., XU, X.Q., MA, C.H., XI, P.W., KONG, D.F. & LEI, Y.A. 2017 Impact of E x B shear flow on low-n MHD instabilities. *Phys. Plasmas* **24** (5), 050704.
- CHU, X., DIAMONDS, P.H. & GUO, Z.B. 2022 SOL width broadening by spreading of pedestal turbulence. *Nucl. Fusion* **62** (6), 066021.
- DUDSON, B.D., UMANSKY, M.V., XU, X.Q., SNYDER, P.B. & WILSON, H.R. 2009 BOUT++: a framework for parallel plasma fluid simulations. *Comput. Phys. Commun.* **180** (9), 1467-1480.
- EICH, T., SIEGLIN, B., SCARABOSIO, A., FUNDAMENSKI, W., GOLDSTON, R.J., HERRMANN, A. AND A. U. TEAM 2011 Inter-ELM power decay length for JET and ASDEX upgrade: measurement and comparison with heuristic drift-based model. *Phys. Rev. Lett.* **107** (21), 215001.
- EICH, T., *et al.* 2013 Scaling of the tokamak near the scrape-off layer H-mode power width and implications for ITER. *Nucl. Fusion* **53** (9), 093031.

- EICH, T., SIEGLIN, B., THORNTON, A.J., FAITSCH, M., KIRK, A., HERRMANN, A. & SUTTROP, W. 2017 ELM divertor peak energy fluence scaling to ITER with data from JET, MAST and ASDEX upgrade. *Nucl. Mater. Energy* **12**, 84-90.
- FAITSCH, M., EICH, T., HARRER, G.F., WOLFRUM, E., BRIDA, D., DAVID, P., GRIENER, M. & STROTH, U. 2021 Broadening of the power fall-off length in a high density, high confinement H-mode regime in ASDEX Upgrade. *Nucl. Mater. Energy* **26**, 100890.
- GARCIA, J., *et al.* 2022 New H-mode regimes with small ELMs and high thermal confinement in the Joint European Torus. *Phys. Plasmas* **29** (3), 032505.
- GOLDSTON, R.J. 2012 Heuristic drift-based model of the power scrape-off width in low-gas-puff H-mode Tokamaks. *Nucl. Fusion* **52** (1), 013009.
- GROEBNER, R.J. & OSBORNE, T.H. 1998 Scaling studies of the high mode pedestal. *Phys. Plasmas* **5** (5), 1800-1806.
- HAHM, T.S. & DIAMOND, P.H. 2018 Mesoscopic transport events and the breakdown of Fick's law for turbulent fluxes. *J. Korean Phys. Soc.* **73** (6), 747-792.
- HARRER, G.F., *et al.* 2018 Parameter dependences of small edge localized modes (ELMs). *Nucl. Fusion* **58** (11), 112001.
- HARRER, G.F., *et al.* 2022 Quasicontinuous exhaust scenario for a fusion reactor: the renaissance of small edge localized modes. *Phys. Rev. Lett.* **129** (16), 165001.
- KOJIMA, A., OYAMA, N., SAKAMOTO, Y., KAMADA, Y., URANO, H., KAMIYA, K., FUJITA, T., KUBO, H., AIBA, N. AND JT-60 TEAM 2009 Fast dynamics of type I and grassy ELMs in JT-60U. *Nucl. Fusion* **49** (11), 115008.
- LI, N.M., XU, X.Q., DIAMOND, P.H., ZHANG, T., LIU, X., WANG, Y.F., YAN, N. & XU, G.S. 2023 How fluctuation intensity flux drives SOL expansion. *Nucl. Fusion* **63**, 124005.
- LI, N.M., XU, X.Q., GOLDSTON, R.J., SUN, J.Z. & WANG, D.Z. 2021 Impact of plasma density/collisionality on divertor heat flux width. *Nucl. Fusion* **61** (2), 026005.
- LI, N.M., XU, X.Q., HUGHES, J.W., TERRY, J.L., SUN, J.Z. & WANG, D.Z. 2020 Simulations of divertor heat flux width using transport code with cross-field drifts under the BOUT plus plus framework. *AIP Adv.* **10** (1), 015222.
- LI, Z.-Y., XU, X.Q., LI, N.M., CHAN, V.S. & WANG, X.G. 2019 Prediction of divertor heat flux width for ITER using BOUT++ transport and turbulence module. *Nucl. Fusion* **59** (4), 046015.
- LOARTE, A., *et al.* 2007 Transient heat loads in current fusion experiments, extrapolation to ITER and consequences for its operation. *Phys. Scr.* **T128**, 222-228.
- LI, N.M., XU, X.Q., ROGNLIEN, T.D., GUI, B., SUN, J.Z. & WANG, D.Z. 2018 Calculation of two-dimension radial electric field in boundary plasmas by using BOUT++. *Comput. Phys. Commun.* **228**, 69-82.
- LI, N.M., XU, X.Q., WANG, Y.F., LIN, X., YAN, N. & XU, G.S. 2022a Impact of pedestal density gradient and collisionality on ELM dynamics. *Phys. Plasmas* **29** (12), 122302.
- LI, N., XU, X.Q., WANG, Y.F., YAN, N., ZHANG, J.Y., QIAN, J.P., SUN, J.Z. & WANG, D.Z. 2022b Characteristics of grassy ELMs and their impact on the divertor heat flux width. *Nucl. Fusion* **62** (9), 096030.
- MAINGI, R., *et al.* 2005 Observation of a high performance operating regime with small edge-localized modes in the National Spherical Torus Experiment. *Nucl. Fusion* **45** (4), 264-270.
- MALONE, R.C., MCCRORY, R.L. & MORSE, R.L. 1975 Indications of strongly flux-limited electron thermal conduction in laser-target experiments. *Phys. Rev. Lett.* **34** (12), 721-724.
- MUKHOVATOV, V., *et al.* 2003 Overview of physics basis for ITER. *Plasma Phys. Control. Fusion* **45**, A235-A252.
- NAZIKIAN, R., *et al.* 2018 Grassy-ELM regime with edge resonant magnetic perturbations in fully noninductive plasmas in the DIII-D tokamak. *Nucl. Fusion* **58** (10), 106010.
- OYAMA, N., *et al.* 2007 ELM frequency dependence on toroidal rotation in the grassy ELM regime in JT-60U. *Plasma Phys. Control. Fusion* **49** (3), 249-259.
- RICCARDI, B., GINIATULIN, R., KLIMOV, N., KOIDAN, V. & LOARTE, A. 2011 Preliminary results of the experimental study of PFCs exposure to ELMs-like transient loads followed by high heat flux thermal fatigue. *Fusion Engng Des.* **86** (9-11), 1665-1668.

- SHIMADA, M., *et al.* 2007 Progress in the ITER physics basis - chapter 1: overview and summary. *Nucl. Fusion* **47** (6), S1-S17.
- STOBER, J., MARASCHEK, M., CONWAY, G.D., GRUBER, O., HERRMANN, A., SIPS, A.C.C., TREUTTERER, W., ZOHM, H. & TEAM, A.U. 2001 Type II ELMy H modes on ASDEX Upgrade with good confinement at high density. *Nucl. Fusion* **41** (9), 1123-1134.
- VIEZZER, E., *et al.* 2023 Prospects of core-edge integrated no-ELM and small-ELM scenarios for future fusion devices. *Nucl. Mater. Energy* **34**, 101308.
- WAGNER, F., *et al.* 1982 Regime of improved confinement and high-beta in neutral-beam-heated divertor discharges of the ASDEX Tokamak. *Phys. Rev. Lett.* **49** (19), 1408-1412.
- WOLFRUM, E., *et al.* 2011 Characterization of edge profiles and fluctuations in discharges with type-II and nitrogen-mitigated edge localized modes in ASDEX Upgrade. *Plasma Phys. Control. Fusion* **53** (8), 085026.
- XIA, T.Y. & XU, X.Q. 2015 Nonlinear fluid simulation of particle and heat fluxes during burst of ELMs on DIII-D with BOUT++ code. *Nucl. Fusion* **55** (11), 113030.
- XIA, T.Y., XU, X.Q. & XI, P.W. 2013 Six-field two-fluid simulations of peeling-ballooning modes using BOUT++. *Nucl. Fusion* **53** (7), 073009.
- XU, X.Q. 2020 Divertor heat flux broadening by grassy ELMs. In *28th IAEA Fusion Energy Conference (FEC)*. Available at: <https://conferences.iaea.org/event/214/contributions/17601/>.
- XU, G.S. 2022 Small-ELM-regime access facilitated by new tungsten divertor on EAST. In *48th EPS Conference on Plasma Physics*. Available at: <https://indico.fusenet.eu/event/28/contributions/264/attachments/278/635/EPSPaper2022-Xu.pdf>.
- XU, G.S., *et al.* 2019a Promising high-confinement regime for steady-state fusion. *Phys. Rev. Lett.* **122** (25), 255001.
- XU, X.Q., LI, N.M., LI, Z.Y., CHEN, B., XIA, T.Y., TANG, T.F., ZHU, B. & CHAN, V.S. 2019b Simulations of tokamak boundary plasma turbulence transport in setting the divertor heat flux width. *Nucl. Fusion* **59** (12), 126039.
- ZHANG, Y., GUO, Z.B. & DIAMOND, P.H. 2020 Curvature of radial electric field aggravates edge magnetohydrodynamics mode in toroidally confined plasmas. *Phys. Rev. Lett.* **125**, 255003.